On the importance of joint mitigation strategies for front, bulk and rear recombination in ultrathin $Cu(In,Ga)Se_2$ solar cells.

Tomás S. Lopes[1,2,3,4], Jessica de Wild[2,3,4], Célia Rocha[1], André Violas[1], José M.V. Cunha[1,5,6], Jennifer P. Teixeira[1], Marco A. Curado[1,7], António J.N. Oliveira[1], Jérôme Borme[1], Gizem Birant[2,3,4], Guy Brammertz[2,3,4], Paulo Fernandes[1,8], Bart Vermang[2,3,4], Pedro M.P Salomé[1,6]*

[1]INL – International Iberian Nanotechnology Laboratory, Avenida Mestre José Veiga, 4715-330 Braga, Portugal

[2]Imec division IMOMEC (partner in Solliance), Wetenschapspark 1, 3590 Diepenbeek, Belgium

[3]Institute for Material Research (IMO), Hasselt University (partner in Solliance), Agoralaangebouw H, Diepenbeek, 3590, Belgium

[4]EnergyVille, Thorpark, Poort Genk 8310 & 8320, 3600, Belgium

[5]i3N, Departamento de Física da Universidade de Aveiro, Campus Universitário de Santiago, 3810-193 Aveiro, Portugal

[6]Departamento de Física, Universidade de Aveiro, Campus Universitário de Santiago, 3810-193 Aveiro, Portugal

[7]University of Coimbra, CFisUC, Department of Physics, R. Larga, P-3004-516 Coimbra, Portugal

[8]CIETI, Departamento de Física, Instituto Superior de Engenharia do Porto, Instituto Politécnico do Porto, Porto 4200-072, Portugal

Abstract

Several optoelectronic issues, such as poor optical absorption and recombination limit the power conversion efficiency of ultrathin Cu(In,Ga)Se_2 (CIGS) solar cells. To mitigate recombination losses, two combined strategies were implemented: a Potassium Fluoride (KF) Post-Deposition Treatment (PDT) and a rear interface passivation strategy based on an Aluminium Oxide (Al_2O_3) point contact structure. The simultaneous implementation of both strategies is reported for the first time on ultrathin CIGS devices. Electrical measurements and 1-D simulations demonstrate that, in specific conditions, devices with only KF-PDT may outperform rear interface passivated based devices. By combining KF-PDT and rear interface passivation, an enhancement in open-circuit voltage of 178 mV is reached over devices that have a rear passivation only and of 85 mV over devices with only a KF-PDT process. Time-Resolved Photoluminescence measurements showed the beneficial effects of combining KF-PDT and the rear interface passivation at decreasing recombination losses in the studied devices, enhancing charge carrier lifetime. X-ray photoelectron spectroscopy measurements indicate the presence of a In and Se rich layer that we linked to be a $KInSe_2$ layer. Our results suggest that when bulk and front interface recombination values are very high, they dominate and individual passivation strategies work poorly. Hence, this work shows that for ultrathin devices, passivation mitigation strategies need to be implemented in tandem.

Keywords : ultrathin CIGS, KF-PDT passivation, Al_2O_3 , recombination mechanisms

Introduction

In order for thin-film $Cu(In,Ga)Se_2$ (CIGS) solar cells to settle with the highest light to power conversion efficiency values among the thin-film technology, strategies to mitigate recombination at the absorber bulk and interfaces had to be developed. In CIGS technology infancy, efficiency enhancements came by improving the architecture developed by Boeing and by optimizing the fabrication process.[1–3] As the technology became more mature, with well-established fabrication process conditions, bulk recombination losses were the major obstacle for further performance improvements. Studies showed the existence of significant bulk and front interface recombination losses in high-efficiency CIGS solar cells (~19 %). [4–6] Heavy alkali incorporation via post deposition treatment (PDT) allowed for the CIGS technology to achieve several efficiency world records[7–11], as it most recently reached 23.35 %.[12] In a PDT process, an alkali metal is deposited after the absorber deposition. Potassium (K) is one of the first successful PDTs in CIGS solar cells.[7] The excellent results of KF-PDT paved the way for other successful alkalis PDT, such as Cs and Rb[9–11,13,14], with a significant amount of studies being conducted to understand the effects of PDT on the CIGS thin film properties[15–20] ,which show standardly enhanced electrical performance.[7,16,21] Several reports show the influence of KF-PDT on the front surface as well as the CIGS bulk properties.[7,15–17,22,23] Looking to the CIGS/CdS interface, KF-PDT leads to a reduction of the amount of Cu and Ga[7,15,16,18] – that promotes Cd filling of copper vacancies (V_{cu}) during chemical bath deposition (CBD) resulting in a higher density of shallow Cd-Cu antisite (Cd_{cu})donors.[7,24] Such effects are linked with reduced front surface recombination leading to increased open-circuit voltage (V_{OC}) and fill factor (FF) values.[7,16] Effects of KF-PDT in the CIGS bulk properties were also reported with

some effects being: KF accumulation at the grain boundaries[16,18,25], reducing tail states, leading to a reduction of localized band-bending, and thus promoting grain boundary passivation.[15]

One of the research lines in the CIGS community is to develop high efficiency ultrathin CIGS solar cells, without compromising performance, in order to save material costs and increase machine throughput.[26] However, in ultrathin CIGS solar cells, rear interface recombination is a major efficiency loss mechanism.[27–29] To reduce rear interface recombination a dielectric nanostructured layer is deposited in-between the CIGS and the Molybdenum (Mo) rear electrode.[30] The dielectric layer: i) neutralizes active recombination centres[31,32]; and ii) creates a built-in electric field – by the presence of fixed charges at the dielectric surface that shields minority carriers.[33] Alumina oxide (Al_2O_3) has shown good results at minimizing rear interface recombination.[34,35] The dielectric layer needs to be patterned, with a point contact structure, to establish electrical contact between the CIGS and rear electrode. Patterning approaches by lithography[36–38] show controlled and reproducible results. Despite its reported success, there is still some debate as to whether this strategy actually benefits the electrical properties of the devices.[39–41] Mainly because of its significant electronic losses at the rear interface, little attention was given to the implementation of PDT in ultrathin CIGS. However, recent reports show the beneficial effects of KF-PDT in ultrathin CIGS solar cells.[21,42] With KF-PDT implementation, front interface and bulk recombination losses will be potentially covered in ultrathin CIGS solar cells. The conjugation of KF-PDT with rear interface passivation is yet to be applied in ultrathin CIGS solar cells. Both treatments may enable the mitigation of front, bulk and rear interface recombination mechanisms, allowing for an enhancement of ultrathin CIGS solar cells electrical performance.

In this work, we present the study of the electrical influence of PDT together with a rear-nano-patterned dielectric layer on ultrathin CIGS solar cell. Three type of devices were produced that incorporate different passivation strategies: i) only KF-PDT; ii) only rear interface passivation and; iii) both passivation strategies. Electrical measurements, together with electrical simulations, modelled the effect of PDT and rear interface passivation on the devices optoelectronic properties. X-ray photoelectron spectroscopy was used to study the elemental composition at the CIGS/CdS interface. Time-Resolved Photoluminescence (TRPL), 1D simulation and AC circuit fitting analysis were used to study the effect of KF-PDT and rear interface passivation on the recombination mechanisms.

Experimental section

An illustrative representation of the fabricated set of ultrathin CIGS based devices is shown in Figure 1: i) with KF-PDT, named PassKF (Figure 1 a)), ii) with only an Al_2O_3 dielectric layer, named PassAl_2O_3 (Figure 1 b)), and iii) with the Al_2O_3 dielectric layer and KF-PDT, named DoublePass (Figure 1 c)). A 20 nm Al_2O_3 layer was deposited by atomic layer deposition (ALD), directly on the rear contact, Mo. To establish the electrical contact between the CIGS and Mo, the dielectric layer was nano-patterned with point contacts by electron beam lithography followed by Reactive Ion Etching (RIE). The point contacts have 200 nm in diameter with a 2 μm pitch (centre to centre) in a quadratic array. A detailed process flow for the patterning approach can be found elsewhere.[36,43] Before the CIGS growth, 7 nm of NaF was evaporated on all substrates ensuring Na supply as the out-diffusion from the SLG might be blocked by the passivation layer.[44,45] The CIGS layer was grown using a 3-stage co-evaporation step. The co-evaporation processes needed to be adjusted to account for the ultrathin CIGS layer. It must be

highlighted that the 3-stage process used in this work has not yet been optimized for ultrathin devices. This procedure is highly sensitive to variation in process conditions such as thickness, temperature, pressure, just to name a few parameters.[45] The 3–stage co-evaporation lead to a small in depth Ga grading that was measured by glow-discharge optical emission spectroscopy (GDOES), in a standard ultrathin CIGS solar cell. All devices underwent the same CIGS evaporation run with an estimated CIGS thickness of 525 nm and composition values of [Cu]/([Ga] + [In]) ~ 0.8 and [Ga]/([Ga] + [In]) ~ 0.3, as measured by X-ray fluorescence (XRF). After the CIGS growth, a KF-PDT was applied to PassKF and DoublePass. The process was done, employing the optimized conditions by de.Wild *et al.*[42,46], by spin coating 0.2 Molarity of KF at room temperature (RT) followed by an anneal in a N_2 atmosphere at 613.15 K. The devices were finalized with the deposition of a stack of CdS/i-ZnO/ZnO:Al/Ni-Al-Ni, with the same process conditions as described elsewhere.[47] 12 solar cells were made for each type of devices with an area of 0.5 cm^2 defined by mechanical scribing.

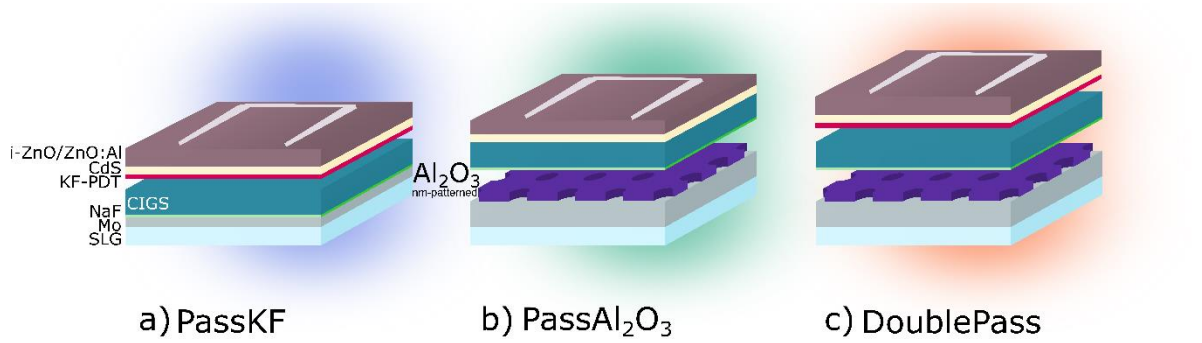

Figure 1 - Illustrative representation of the fabricated devices: a) device with only PDT, PassKF; b) device with only rear interface passivation layer, PassAl_2O_3; c) device with both treatments, KF-PDT and rear interface passivation, DoublePass. Layers not at scale.

The solar cell current density against voltage (J-V) and the temperature dependent J-V (J-V-T) measurements were conducted in a home-built system with a four-point probe. The J-VT

measurements were conducted in the temperature range between 100-303.15K with liquid nitrogen being used as a cooling agent. External quantum efficiency (EQE) measurements were performed on a home-built system, with the short-circuit current density value (J_{SC}) being corrected to the EQE spectra. Capacitance-voltage-frequency (C-V-f or C-V) and capacitance–conductance-frequency (C-G-f) measurements were conducted with a precision LCR meter (Agilent E4980 A). The C-V-measurements were taken from -0.6 to 0.8 V with a fixed 10 kHz frequency with a V_{RMS} of 30 mV, at RT in the dark. C-G-f measurements were performed at 0 V bias from 20 Hz to 1 MHz with a V_{RMS} of 30 mV, at RT in the dark. Time-Resolved Photoluminescence (TRPL) was measured at RT with a photospectrometer Picoquant with a TimeHarp 260 single photon counter. The excitation intensity was approximately 0.1 Wcm^{-2}, repetition rate 3 MHz, and excitation wavelength of 532 nm. EQE and J-V representative curves where chosen based on the averaged values of the individual solar cells in each device. The XPS measurements was performed on an ESCALAB 250 Xi Thermo Scientific, equipped with a monochromatic Al K_{α} source (1.487 KeV). The depth profile etch was divided in three parts; a) The first etch was to remove the ZnO layer, with a ion gun energy of 4000 eV; b) to reach a clear signal of the CdS layer the energy gun was decreased to 500 eV; c) finally to understand the elemental composition on the interface between CIGS and CdS we used energy gun with 200 eV. Since we want to quantify each element the data was acquired with a hemispherical pass energy of 20 eV. A Avantage (Thermo Fisher Scientific) software was used to fit the peaks with a smart background using a Laurence-Gaussian function.

Electrical simulations of the fabricated devices were conducted with SCAPS 1-D software[48], with Table 1 and 2 showing the most important input values, based on measured and literature values.[49–51] The shunt conductance (R_{shunt}) and the series resistance (R_{series}) were extracted from

J-V measurements, with the net free carrier concentration (N_{cv}) extracted from C-V measurements. The CIGS bandgap energy (E_g) in depth variation was calculated through Eq. 1 based on the Ga profile measured by GDOES[50]:

$$E_g = 1.01 + 0.626 * GGI - 0.167 * GGI * (1 - GGI) \quad (1)$$

From (1), we obtained a small bandgap variation, with an in depth variation of 1.22->1.16->1.22 eV at the front and rear interface, respectively. Since all devices were grown in the same evaporation run, we consider the E_g in depth profile to be the same for all devices. The optical properties of the CIGS layer were measured using an in-house ellipsometry equipment. For the CdS, i-ZnO and ZnO:Al, the optical properties were extracted from the literature[52,53].

Table 1 - SCAPS electrical parameters used for the CIGS, CdS, i:ZnO and ZnO:Al layers devices simulations. The CIGS E_g values correspond to the obtained Ga grading. χ_e refers to electron affinity. N_D refers to shallows donors concentration, N_{cv} is the net free carrier concentration.

Parameter	**CIGS**	**CdS**	**i:ZnO**	**ZnO:Al**
E_g (eV)	1.22->1.16->1.22 (experimental in depth variation)	2.4 [50]	3.3 [50]	3.3 [50]
χ_e (eV)	4.31->4.38->4.301 (experimental in depth variation)	4.11 [50]	4.31 [50]	4.31 [50]
N_D shallow donor (cm^{-3})	10 x 10^1	1 x10^{16} [49,50]	1 x10^{17} [49,50]	1 x10^{20} [49,50]

N_{CV} **(cm^{-3})**	PassKF:6.05x 10^{15} PassAl$_2$O$_3$: 31.0x 10^{15} DoublePass: 21.0x 10^{15}	0	1 x10^{17} [49]	0

Table 2 – Parameters corresponding to the defects introduced in our model. Defect 1 corresponds to double donor In_{Cu}. N_t corresponds to the correspondent defect concentration, $\sigma_{e/H}$ is the electron and hole capture cross section with E_t being the defect energy, E_{VB} and E_{CB} correspond to the valence band and conduction band energies of the CIGS layer. Defect 2 corresponds to the double acceptor Cu_{In} defect, with Defect 3 being half acceptors and half donors to simulate the electronic activity at the CIGS grain boundaries.

	Type	**Distribution**	N_t **(cm^{-3})**	$\sigma_{e/H}$ **(cm^2)**	E_t
Defect 1 [49,51]	Double Donor	Single	1x10^{13}	1x10^{-15}/1x10^{-13}	E_{CB}-0.24, E_{CB} -0.34
Defect 2 [49,51]	double acceptor	single	1x10^{13}	1x10^{-13}/1x10^{-15}	E_{VB}+0.29, E_{VB} + 0.58
Defect 3 [54]	Acceptor/donor		PDT- 5.0 x10^{15} No PDT 15x10^{15}	1x10^{-15}/1x10^{-15}	E_{VB}+0.27

Results

Representative illuminated and dark J-V curves, and EQE spectra are shown in Figure 2 a) and b), respectively with the average figures of merit values obtained from the J-V measurements are

summarized in Figure 2 d), as well as the diode quality factor, *A*, and saturation current density, J_0 — calculated through the dark J-V curves following the procedure by Hegedus *et al*, taking into account the devices' R_{series} and R_{shunt}.[55] From the J-V curves analysis, we immediately note that the PassKF device shows signs of shunting problems on the illuminated J-V curve. However, the dark J-V curve does not show the same behavior indicating that the device is affected by voltage-dependent current collection (VDCC)[34,56]. Ultrathin devices without rear passivation often show VDCC compatible with a high rear interface recombination.[34,36] Furthermore, DoublePass device shows a roll-over behavior in the J-V curve leading to a higher series resistance for this device. Roll-over behaviors usually indicates an interface barrier.[57,58] Additionally, we note that the shunt resistance increases with the application of the dielectric layer. This increase is likely related to a reduction of shunt paths present in the device prevalent in ultrathin CIGS solar cells. [59–61] The EQE analysis shows a small increase in the 400 - 500 nm range for the devices that underwent the PDT treatment in comparison with PassAl_2O_3. This enhancement is likely due to a thinner CdS layer for these devices, most likely caused by KF-PDT.[7] The devices with the rear passivation layer show an increase of the EQE in the wavelength region values between 550 and 1100 nm in comparison with PassKF. The EQE enhancement in the two rear passivated devices leads to an increase in the short-circuit current density (J_{SC}) values, compatible with an increase in the rear optical reflection as well as an effective passivation effect.[30,35,36 55] DoublePass device shows higher V_{OC} and efficiency values than PassAl_2O_3 and PassKF. DoublePass V_{OC} values show an increase of 85 mV (abs) over PassKF and 178 mV (abs) over PassAl_2O_3 ultimately leading to a 2.2 % and 2.3 % increase in power conversion efficiency values, over PassKF and PassAl_2O_3 respectively. Notwithstanding, the enhancement in V_{OC}, the DoublePass J_{SC} and *FF* values does not show a significant increase

over PassAl_2O_3, indicating that the KF-PDT process is not improving carrier collection. The PassAl_2O_3 device, which has lower V_{OC} than Pass KF devices, shows similar efficiency values to PassKF. So, the impact of individual passivation strategies leads to similar solar cells performance. The V_{OC} increase by DoublePass indicates a decrease on the impact of the recombination losses, attained by the joint application of a rear Al_2O_3 passivation layer together with the KF-PDT. In fact, this claim is supported by the J_0 values, as DoublePass shows the lowest J_0 among the fabricated devices. Considering the Shockley-Read-Hall (SRH) recombination model [62,63], the A values of PassAl_2O_3, PassKF and DoublePass (2.3 ± 0.5 vs 1.7 ± 0.3 vs 1.3 ± 0.4, respectively) indicates different locations of the dominant recombination mechanism in the active layer: from the space charge region to the quasi neutral region, respectively.[64] From the normalized V_{OC} vs T analysis we extracted the activation energy (E_A) of the saturation current, by performing a linear fit of the V_{OC} in the high temperature range and verifying its value at 0 K.[55] For the studied devices, the E_A value is similar to the bandgap energy value for DoublePass (1.25 eV) and lower than the bandgap value for PassKF and PassAl_2O_3 (0.84 and 0.60 eV, respectively).

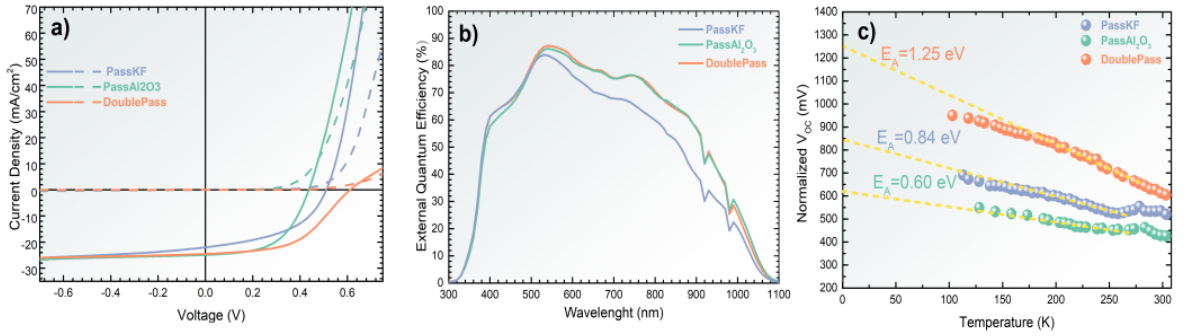

d)	V_{OC} (mV)	J_{SC} (mA/cm²)	FF (%)	Eff (%)	A	J_0 (mA/cm²)	R_{shunt} (Ω.cm²)	R_{Series} (Ω.cm²)
PassKF	519 ± 45	23.2 ± 1.5	49.0 ± 4.9	5.7 ± 1.6	1.7 ± 0.3	(8.8 ± 0.2) x 10^{-4}	215 ± 70	0.47± 0.24
PassAl$_2$O$_3$	426 ± 16	25.4 ± 0.3	51.4 ± 2.6	5.6 ± 0.5	2.3 ± 0.5	(2.9 ± 2.6) x 10^{-2}	495 ± 75	1.27 ± 0.09
DoublePass	604 ± 20	25.5 ± 0.7	51.3 ± 2.4	7.9 ± 0.7	1.3 ± 0.4	(9.1 ± 0.1) x 10^{-5}	617 ± 173	2.96 ± 2.23

Figure 2 – a) Representative dark (dashed) and Illuminated (solid) J-V curves; b) EQE curves for the fabricated devices; c) V_{OC} vs T curves; and d) Averages and standard deviation values of the devices figures of merit for 12 solar cells per device.

C-V measurements were conducted on the studied devices to understand the influence of both passivation strategies on the net free charge carrier concentration (N_{CV}), the CIGS space charge region width (w) and the built-in potential (V_{bi}) values, calculated using well-known procedure[65,66] and presented in the Table 3. The PDT treated devices present the lowest N_{CV} and largest w values. KF-PDT promotes Cd filling of the V_{CU} acceptors, leading to an increase of shallow donors Cd_{Cu} density, promoting a larger space charge regions and lower values of net free carrier concentration, compatible with trend obtained in the studied devices.[67] The V_{bi} value of PassKF and DoublePass devices is lower than the measured V_{OC} value, indicating the presence of an electron barrier at the buffer or window layer.[68] The existence of an electron barrier limits the FF value, with little influence on the V_{OC} value.[68] So, the V_{bi} values lower than V_{OC} and the

similar *FF* values for PassKF and DoublePass devices, indicates the active role of KF-PDT in the emergence of such electron barrier.

Table 3 - N_{CV}, w and V_{bi} average and standard deviation values.

Devices	N_{CV} **(x 10^{15}cm^{-3})**	w **(nm)**	V_{bi} **(mV)**
PassKF	(6 ± 3)	375 ± 80	453 ± 65
PassAl$_2$O$_3$	(31 ± 6)	167 ± 24	492 ± 61
DoublePass	(21 ± 6)	215 ± 24	548 ± 106

The equivalent circuit fitting analysis of the admittance data allows the study of the device AC response. The impedance data extracted from admittance measurements were fitted using several equivalent circuits through the ZSimpWin 3.50 software.[69] A detailed explanation of the procedure used to consider the most accurate equivalent circuit for each device can be found elsewhere.[70] Figure 3 a), b) and c) shows the equivalent circuit for the developed devices, PassKF, PassAl$_2$O$_3$ and DoublePass, respectively, with Figure 3 d) showing the fitted and estimated parameter for each equivalent circuit.

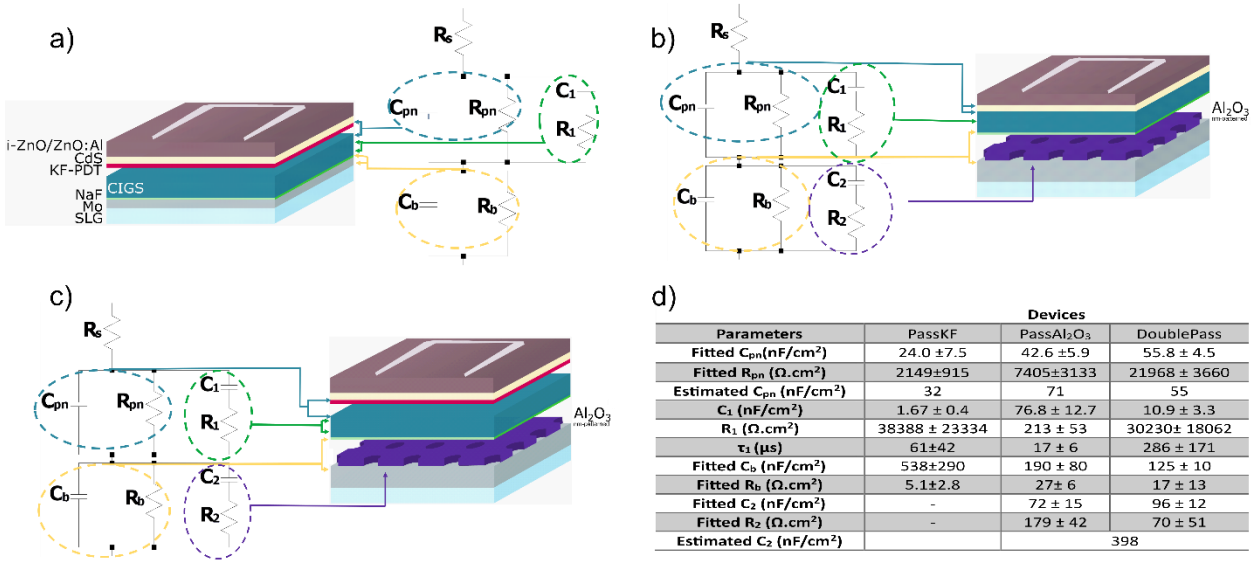

	Devices		
Parameters	PassKF	PassAl$_2$O$_3$	DoublePass
Fitted C_{pn}(nF/cm²)	24.0 ±7.5	42.6 ±5.9	55.8 ± 4.5
Fitted R_{pn} (Ω.cm²)	2149±915	7405±3133	21968 ± 3660
Estimated C_{pn} (nF/cm²)	32	71	55
C_1 (nF/cm²)	1.67 ± 0.4	76.8 ± 12.7	10.9 ± 3.3
R_1 (Ω.cm²)	38388 ± 23334	213 ± 53	30230± 18062
τ_1 (μs)	61±42	17 ± 6	286 ± 171
Fitted C_b (nF/cm²)	538±290	190 ± 80	125 ± 10
Fitted R_b (Ω.cm²)	5.1±2.8	27± 6	17 ± 13
Fitted C_2 (nF/cm²)	-	72 ± 15	96 ± 12
Fitted R_2 (Ω.cm²)	-	179 ± 42	70 ± 51
Estimated C_2 (nF/cm²)		398	

Figure 3-Equivalent electrical circuits for: a) PassKF; b) PassAl_2O_3; and c) DoublePass); d) Fitted and estimated parameters average and standard deviation values for the equivalent circuits of all devices.

As shown in Figure 3, each electrical component represents a different type of interface and/or property in the solar cell.[71–74] *Rs* represents the solar cell series resistance induced by front and rear contacts.[70,72] The space charge region is modelled by C_{pn} and R_{pn} in parallel that represents the p-n junction capacitance and resistance, respectively.[70,75] The rear electrical contact is represented by a rear contact capacitance (C_b) and a rear contact resistance (R_b) in parallel.[72,75] A C_i capacitance is in series with a resistance R_i it represents a measure anomaly, in the AC regime, that may be associated with a defect trap level.[71,76,77] The i=1,2 is the representation of different anomalies present in the assigned device.[66,71] For each C_i-R_i connection in series there is an associated τ_i representing a characteristic lifetime. In the case of a trap, it corresponds to the charging/discharging time characteristics of the associated trap level.[71,76,77] From the fitted circuits, for the rear passivated devices, we note two branches with a capacitance in series with a resistance: C_1-R_1 and C_2-R_2. In the literature, C_1-R_1 is associated with defects levels in the absorber bulk.[70,78,79] The C_1-R_1 connection is present in all circuits, meaning that in our studied devices, the passivation strategies implemented were not able to mitigate such defect level. The C_2-R_2 is only absent for the device without the Al_2O_3 layer. Thus, we attribute the C_2-R_2 to a frequency response of the dielectric layer.[70]

The estimated capacitance values were calculated for comparison with the fitted values, in order to validate our results, using the well-known capacitance equation:[80]

$$C = \frac{\varepsilon_0 \varepsilon A}{d} \quad (2)$$

where ε_0 is the vacuum permittivity, ε the dielectric constant, A the solar cell area and d the space charge region width or the Al_2O_3 thickness. The vacuum permittivity has the value of 8.8 x 10-12 F/m; the considered dielectric constant for CIGS is 13.45[81] , and for Al_2O_3 is 9[82]. The fitted C_{pn} values for PassKF (24.0 ± 7.5 nF/cm^2) and DoublePass (55.8 ± 4.5 nF/cm^2) are in good agreement with the calculated ones (32 nF/cm^2 and 55 nF/cm^2 respectively), ensuring that the chosen equivalent circuit has physical meaning. However, the fitted C_{pn} for PassAl_2O_3 (42.6 ± 5.9 nF/cm^2) device is lower than the estimated one (71 nF/cm^2). Such difference may be explained by a possible change in the CIGS refractive index, something not completely to be discarded due to the extensive known effect of the PDT process. The extracted R_{pn} values for PassAl_2O_3 and DoublePass increase when compared to PassKF device. The increase of R_{pn} reveals that the dielectric layer is effectively mitigating shunts paths, which are common in ultrathin CIGS solar cells.[38,59–61] Regarding the C_1-R_1 branch, DoublePass shows a τ_1 value (286 ± 171 μs) significantly higher than the PassAl_2O_3 (17 ± 6 μs), and the PassKF (61 ± 42 μs). The time constant, τ_1 the time of capture and emission of an electron.[76] Thus, a higher τ_1 corresponds to a lower recombination velocity. The τ_1 trend suggests that: i) KF-PDT mitigates recombination at the absorber bulk, since devices with KF-PDT show higher τ_1 value than the device without PDT; and ii) both passivation strategies have a compound effect at addressing losses in the absorber bulk. We observe that C_b values decrease by adding the rear interface passivation layer to the device architecture, indicating that the dielectric introduction is changing the rear contact, which may be related with the $MoSe_2$ layer.[57] Moreover, an increase in R_b values is also observed for PassAl_2O_3 and DoublePass. Such increase is due to the fact that these

devices only have 1 % of contacting area at the rear surface, which likely increases contact resistance suggesting that the point contact pattern needs optimization. The presence of C_2-R_2 is due to a response of the nano-patterned dielectric layer to the measurement frequency. We note, that the calculated C_2 capacitance is significantly lower than the estimated C_2 for PassAl_2O_3 and DoublePass devices. To calculate the Al_2O_3 capacitance we assumed a conformal non-interrupted layer, even though the developed Al_2O_3 layer covers 99 % of the surface area. Hence, the difference between the estimated and fitted capacitance values of C_2, could be attributed to the nano-patterning of the Al_2O_3 and to different properties of such thin layer from the ones used for the extraction of the dielectric constant.

The measurements of the carrier lifetime by means of TRPL allow for a better understanding of the impact of the two different passivation strategies in the recombination losses of the studied devices[83–85] as shown in Figure 4. The DoublePass decay is significantly longer than both PassKF and PassAl_2O_3 devices, which show similar decay curves. The performed fits considered the deconvolution of the instrumental response. The three devices' TRPL decays follow the same trend, being well described by a biexponential function with two characteristic decay lifetimes: a fast component, often linked to charge separation; and a slower one linked to recombination mechanisms.[86–88] The latter component is the one that allows for insight into the passivation impact on the optoelectronic properties of the devices.[86–88] However, the determination of the factor that defines the TRPL quenching – process that sharply reduces luminescence – is not that straightforward. Since TRPL measurements were carried in final devices, the decay curves can be influenced by different physical factors, including diffusion processes, carrier drift, interface and/or bulk recombination, Ga gradient, among others, which makes the precise determination of the TRPL quenching origin quite puzzling.[85,86] Notwithstanding, the obtained slower lifetime

decay values were 0.5 and 0.40 ns for PassKF and PassAl$_2$O$_3$ device, respectively, and 12.6 ns for DoublePass device. It has been shown in CIGS based solar cells a correlation between recombination mechanisms (lifetime decays) and V_{OC} values.[84,89,90] In fact, from the TRPL experimental conditions it is expected that interface recombination mechanisms have a high impact in the TRPL decay, leading to sharply reduced lifetime decay values, like the ones obtained in PassKF and PassAl$_2$O$_3$ devices. At room temperature the SRH recombination mechanism may be responsible for the TRPL quenching, with deep defects contributing for the TRPL quenching and shallow defects contributing for the material conductivity. For the PassKF device the location for the dominant SRH recombination mechanism is ambiguous, as it could be located at the space charge region and even at the interface. Nonetheless, TRPL results, in addition to E_A and A values, for the PassKF and PassAl$_2$O$_3$ devices are compatible with interface recombination and again the combined impact of the two treatments provide for a significant improvement in the DoublePass device.

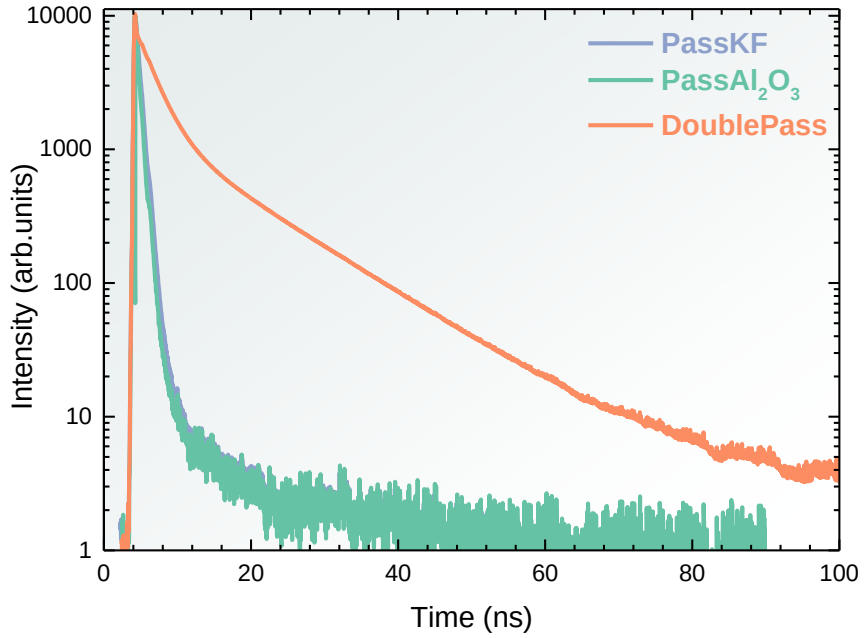

Figure 4 – Normalized TRPL decays at room temperature for all the CIGS studied devices. The decay lifetime was 0.5 ns for PassKF devices, 0.4 ns for PassAl_2O_3 and 12.6 ns for DoublePass device.

To better understand the electrical effects of KF-PDT and rear interface passivation, electrical modelling of the fabricated structures was conducted through SCAPS 1-D simulation. Table shows the simulated J-V figures of merit for the studied devices. The SCAPS baseline model used in this paper was based on parameters used by T.M. Friedlmeier *et al.*[49], J. Petterson *et al.*[50], as well as the measured R_{series}, R_{shunt} and N_{CV} values. The modelled effects of PDT were based on the reported effects on the front interface and in the CIGS bulk [7,15,16,54,91]. In particular, we added the following effects related to KF-PDT: i) grain boundary electrical activity by introducing an defect 270 meV above the valence band with a concentration of 5.0 x 10^{15} cm^{-3} [15,54] and; ii) reduction of the acceptor density at the CIGS/CdS interface to simulate the effect of increased donor defects.[16,17,91] To simulate the effect of rear interface passivation, we varied the surface recombination velocity (SRV) value, as follows: since ultrathin CIGS devices have high rear interface recombination, we attributed an SRV value of 10^7 $cm.s^{-1}$ for PassKF device and 10^2 $cm.s^{-1}$ for the devices with rear interface passivation, according to previous works.[30,36,92] The rear optical reflection was set at 40 % for PassKF device and 50 % for PassAl_2O_3 and DoublePass in order to have a good correlation between the simulated and measured J_{SC}. The initial simulated *FF* for PassKF and DoublePass device was 15 % and 13.5 % higher than the experimental ones, with only PassAl_2O_3 having a good correlation. The R_{shunt} and R_{series} from J-V measurements were taken as an input parameter in order to approach the FF value to the experimental one for the model. The higher simulated *FF* value, for PassKF and DoublePass, is compatible with the existence of the above stated barrier at the front interface that lowers the

experimental FF. In fact, studies report the formation of a K-In-Se_2 (KIS) layer[93–95] that was linked to a blocking behavior.[96] The high bandgap of the KIS layer (2.55 eV) is responsible for the blocking behavior as it increases the conduction band-offset between the CIGS and CdS.[96] In order to discuss the existence of such layer in KF-PDT devices, an extra set of simulations were performed in which we introduced the KIS layer in between the CIGS and CdS and varied its thickness. Figure 5 shows the PassKF simulated J-V curves with an additional KIS layer, with different thickness. The results show that just a 5 nm thick KIS layer is sufficient for a 7 % drop in the *FF* value. Further increasing the thickness will lead to a small decreases in the *FF* value, with a roll-over appearance for a KIS thickness of 50 nm. The inclusion of a KIS layer in our model lead to an approximation of the simulated and experimental FF for the KF treated devices. With regards to the difference between the simulated and experimental V_{OC} for the PassKF and PassAl_2O_3 devices an higher impact of the recombination losses. For all devices, the simulated J_{SC} values show an excellent correlation with the experimental J_{SC} values. The electrical simulations show that with the introduced KF-PDT leads to higher electrical performance than using only rear interface passivation. Regardless of the discrepancies between simulations and the J-V measurements, the electrical simulations show the same electrical trends observed by J-V measurements. This could be an indication that, the KF-PDT and rear interface passivation effects were correctly modelled allowing to discuss the losses mechanisms of each devices, which was the main objective of the behind the electrical simulations, rather than reaching a precise match that is quite complex for cells at this performance stage.

Table 4 - Simulated J-V figures of merit for the studied devices. In brackets, it is represented the variation with the corresponding average experimental J-V parameters for a better comparison.

Devices	**V_{OC} (mV)**	**J_{SC} (mA/cm^2)**	**FF (%)**	**Eff** (%)
PassKF	617 (+98)	23.9 (+0.7)	57.8 (+6.5)	8.5 (+2.8)
PassAl_2O_3	612 (+186)	25.1 (-0.3)	54.3 (+2.9)	8.3 (+2.7)
DoublePass	657 (+53)	25.4 (-0.1)	58.8 (+ 7.5)	9.7 (+1.8)

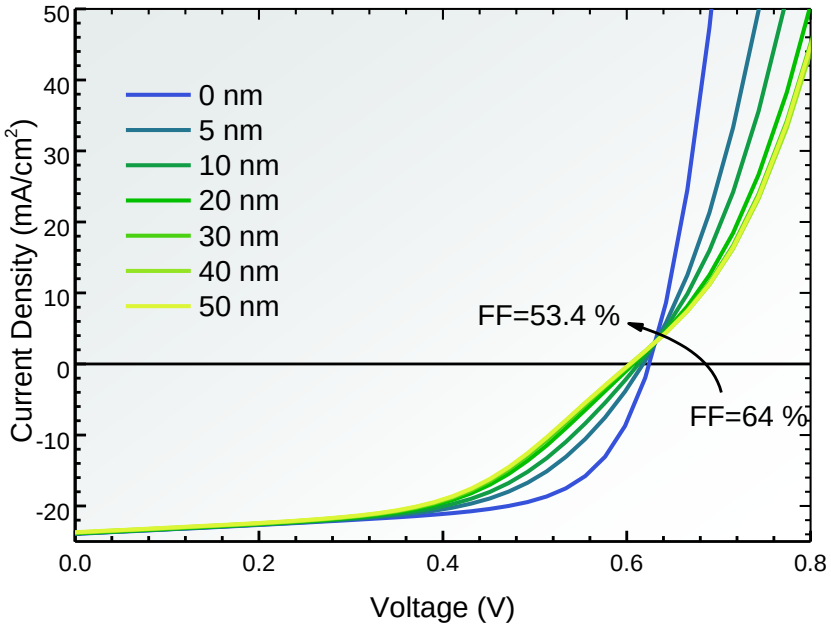

Figure 5 – Simulated J-V curves of PassKF device with a thickness variation of the KIS layer.

The electrical and simulation results for the samples with PDT suggest a presence of an electron barrier between the CIGS and CdS that we associated to a KIS layer. To check the presence of a KIS layer we performed a depth profile XPS analysis on the DoublePass

device. The XPS analysis allows for a deeper understanding of the elemental distribution in-between the CdS and CIGS layers, with the results being shown in Figure 6. Figure 6 a) shows an elemental variation, as the etch level increases, for the CdS and CIGS elements, as it Figure 6 b) shows only the elements present in the CIGS layer. Figure 6 c) shows the peak intensity as well as the curve fitting of the individual CIGS elements with increasing etch levels. From Figure 6 a) we notice that as the etch level increases the atomic % of Cd and S decreases while the atomic % of Cu, In, Ga, and Se increases, suggesting that the studied region describes the CIGS/CdS interface. From Figure 6 b) the individual CIGS elements start to appear in different etch levels, which is seen in Figure 6 c) as we are able to fit the In 3d peak from etch level 0 and Se 3d from etch level 7, whereas we were only able to fit the individual peak for Cu 2p and Ga 2p at etch level 14 and 13, respectively. In the literature, the analysis of the atomic percentage at the interface of CIGS/CdS, without PDT, usually founds that the CIGS elements appear at the same etch level [97,98], or even detect Cu first, due its diffusion towards the CdS.[98–100] The fact that for our device the In 3d peaks and Se 3d peaks are the first elements to appear suggests that the interface is rich in In and Se, and that Cu and Ga are absent, could be an indication of the KIS layer presence. The depth profile analysis did not detect a trustful K signal. The detection of a KIS layer in finalised CIGS devices is not straightforward as KF-PDT may react with Cd during CBD.[95,101] With discrepancies being found in the literature, where studies showed that the KIS layer could still be detected after a thin CdS layer deposition[7], others could not detected K after the CBD treatment, while other suggested that the KIS layer may partly dissolve itself during the CBD process[95] leading to difficulties at identifying it. The etching performed in the XPS measurements during the depth profile study, may promote alkali

diffusion towards the CIGS bulk, given its high mobility[102–104]. Thus, this effect may occurs in our devices leading to the absence of a trustful K signal. Nonetheless, our XPS results showed that In and Se were the first elements to be detected with a clear signal at the interface between CIGS and CdS, indicating an interlayer presence between the CdS and CIGS layer. Given that the electrical measurements and the 1-D simulation point to a formation of a barrier between CIGS and CdS, as XPS results point to an interfacial region rich in In and Se, such interlayer may indeed be a KIS layer, which the the presence is commonly associate to KF-PDT.

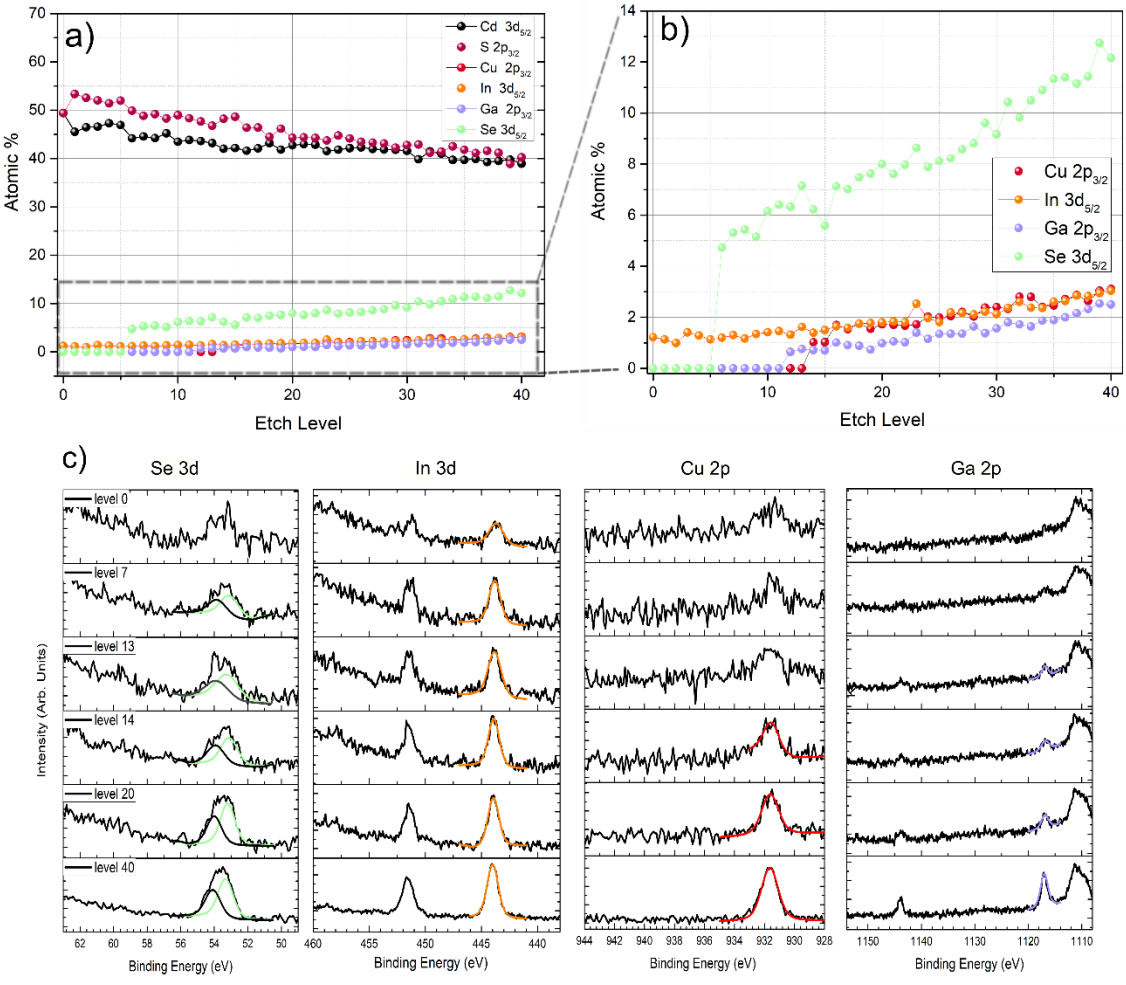

Figure 6 - a) XPS depth profile with increasing etch level of the CIGS and CdS elements

at the CIGS/CdS interface; b) XPS depth profile of the CIGS elements ; c) Individual XPS Spectra of Se 3d, In 3d, Cu 2p, Ga 2p. The color lines indicate the fit performed to the individual peak.

DISCUSSION

We show that only with the application of both treatments the maximum potential of a solar cell is revealed as, individually, each of the improvements is not enough to counter for all the dominant losses. As shown in Figure 2a) DoublePass device shows the presence of a roll-over behavior in its representative J-V curve, common in devices with insufficient Sodium (Na) as the passivation layer acts as a Na diffusion barrier [44,105]. However, since all devices had a pre-deposition of 7 nm of NaF and only DoublePass shows the roll-over and, SCAPS simulation hinted at the presence of a blocking layer at the front interface and the XPS analysis indicated the presence of an extra layer at the CIGS/CdS interface, the roll-over anomaly could be due to the conjugation of the dielectric blocking Na diffusion and a presence of a KIS layer at the front interface. The KIS layer is linked with a blocking behavior as it increases conduction band offset between CIGS and CdS.[96] In fact, the presence of a blocking layer is also hinted by the V_{bi} values extracted from the C-V measurements, which were lower than the measured V_{OC} values for the KF-treated devices. The XPS analysis hinted at the presence of an In and Se rich layer at the interface. Together with C-V measurements and the electrical simulation such layer could indeed be a KIS layer. Thus, the KIS layer present in our devices could be responsible for the low *FF* values as well as the V_{bi} values lower than V_{OC} for the PassKF and DoublePass device.[68] Figure 7 shows the difference between the measured and simulated figures of merit for the developed devices. Note that, the simulated *FF* value for PassKF and DoublePass could only be approximated to their experimental values with the incorporation of a KIS layer at the front

interface. The V_{OC} value of the DoublePass device is the highest among the studied devices and the J_0 value is the lowest, suggesting that several recombination mechanisms are mitigated compared to the other studied devices, which is supported by the highest charge carrier's lifetime value observed in TRPL. The E_A value gives information of what is the type of dominant SRH recombination[55,62,63]: if $E_A \sim E_g$, the dominant recombination mechanism is present in the CIGS bulk; and if $E_A < E_g$, we have a dominant interface recombination. For the PassKF and PassAl_2O_3, the E_A value is lower than the bandgap value, with together with A values indicate that for devices bulk recombination is not the dominant mechanism.[55] By linking the decay lifetime with recombination in the devices[84,86,89], the TRPL measurements suggest that from the low carrier lifetime of PassKF and PassAl_2O_3 devices, that front interface recombination is the dominant recombination mechanism. For DoublePass device, the electrical and optoelectronic results, E_A = 1.25 eV, A = 1.3 and longer TRPL decay time, support a dominant SRH recombination in the absorber bulk. So, these results suggest that the implementation of both passivation strategies were able to neutralize dominant interface recombination mechanisms present in PassKF and PassAl_2O_3. The A value of PassAl_2O_3 higher than 2 points that the dominant recombination mechanism is not governed by the SRH assumptions[92,106] , but other model should be consider such as multi-step recombination fluctuating potentials or tunneling effect.[106,107]

All in all, we show that, in order to have proper rear interface passivation gains, the CIGS/CdS interface and the bulk quality of CIGS must be treated, otherwise a rear interface passivation strategy does not lead to optoelectronic gains as other losses would still be dominant. Electrical and optoelectronic results suggest that rear interface recombination in the devices is ineffective when front interface or bulk recombination values are very high and dominant. Both strategies

must be coupled together to minimize recombination losses, thus maximizing the electrical performance of ultrathin CIGS solar cells.

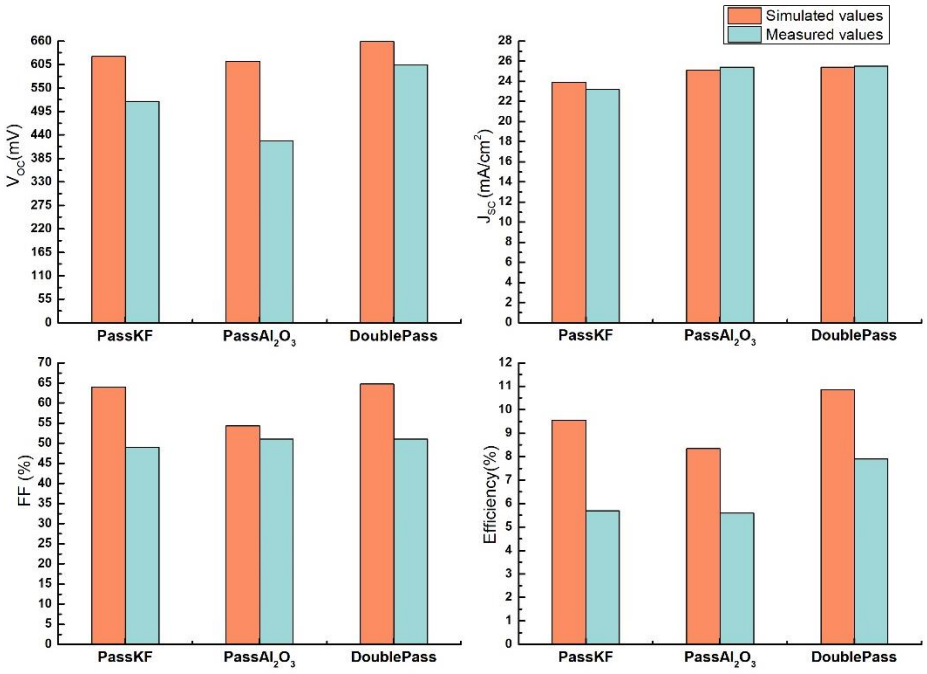

Figure 7 - Comparison between the simulated and measured solar cells figures of merit of the fabricated devices.

Conclusion

A Rear interface passivation strategy and a post-deposition treatment were for the first time applied at the same time in ultrathin CIGS solar cells. Rear interface passivation was achieved with the introduction of a 20 nm nano-patterned Al_2O_3 layer with the PDT being performed with KF. We report, for the first time, the implementation of a KF-PDT treatment together with a rear interface passivation scheme in ultrathin CIGS solar cells. Moreover, we show that only the application of both treatments the maximum potential of a solar cell is revealed as, individually,

each of the improvements is not enough to counter for all the dominant losses. From the studies performed, we conclude that, in order to have significant optoelectronic gains all the recombination mechanisms must be dealt with. The implementation of both strategies leads to significant enhancements of the optoelectronic properties. Despite of the observed improvement, the presence of the roll-over for DoublePass indicates room for further improvements in the KF-PDT and NaF deposition conditions. These findings are corroborated by electrical 1-D simulation together with a XPS analysis that found the presence of a In and Se rich layer that could be responsible for the blocking behavior in our devices. The TRPL decay time of the studied devices was profoundly affected by front interface recombination, as PassKF and PassAl_2O_3 devices show low lifetime values. However, DoublePass showed a significant higher decay time value over the devices with only one treatment, suggesting the advantages of using both passivation strategies. Admittance circuit fitting analysis showed the presence of active recombination channels in the absorber bulk and that KF-PDT is able to reduce its impact. Altogether, our striking results suggest the need to address losses at the front surface and bulk to successfully implement rear interface passivation and that both strategies need to be used in tandem as no silver bullet exist to provide ultrathin solar cells with an unique solution to its drawbacks.

Corresponding Author

Corresponding Author:

Email: tomas.lopes@inl.int

Author Contributions

The manuscript was written through contributions of all authors. All authors have given approval to the final version of the manuscript.

Funding Sources

Fundação para a Ciência e Tecnologia through grants: IF/00133/2015, PD/BD/142780/2018 and SFRH/BD/146776/2019 and projects: PDTC/CTM-CTM/28075/2017, PTDC/FISMAC/29696/2017 and UIDB/04730/2020. European Union's Horizon 2020 through grants nr: 720887 and 715027 The Special Research Fund (BOF) of Hasselt University

Acknowledgements

Fundação para a Ciência e a Tecnologia (FCT) is acknowledged through the project IF/00133/2015, PD/BD/142780/2018 and SFRH/BD/146776/2019. The authors want to acknowledge the European Union's Horizon 2020 research and innovation programme under the agreements no. 720887 (ARCIGS-M project) and agreement No. 715027 .The Special Research Fund (BOF) of Hasselt University, the FCT through the project NovaCell (PDTC/CTM-CTM/28075/2017), and InovSolarCells (PTDC/FISMAC/29696/2017) co-funded by FCT and the ERD through COMPETE2020. P. A. Fernandes would like to acknowledge FCT for the support of the project FCT UIDB/04730/2020.

References

(1) Chen, W. S.; Stewart, J. M.; Stanbery, B. J.; Devaney, W. E.; Mickelsen, R. A. Development of Thin Film Polycrystalline $CuIn_{1-x}Ga_xSe_2$ Solar Cells. In *Photovoltaic specialists conference. 19*; 1987; pp 1445–1447.

(2) Potter, R. R. Enhanced Photocurrent ZnO/CdS/$CuInSe_2$ Solar Cells. *Solar Cells* **1986**, *16*, 521–527. https://doi.org/10.1016/0379-6787(86)90107-9.

(3) Hedstrom, J.; Ohlsen, H.; Bodegard, M.; Kylner, A.; Stolt, L.; Hariskos, D.; Ruckh, M.; Schock, H.-W. ZnO/CdS/Cu(In,Ga)Se_2 Thin Film Solar Cells with Improved Performance. In *Conference Record of the Twenty Third IEEE Photovoltaic Specialists Conference - 1993 (Cat. No.93CH3283-9)*; 1993; pp 364–371. https://doi.org/10.1109/PVSC.1993.347154.

(4) Contreras, M. A.; Ramanathan, K.; AbuShama, J.; Hasoon, F.; Young, D. L.; Egaas, B.; Noufi, R. SHORT COMMUNICATION: ACCELERATED PUBLICATION: Diode Characteristics in State-of-the-Art ZnO/CdS/Cu($In_{1-x}Ga_x$)Se_2 Solar Cells. *Progress in Photovoltaics: Research and Applications* **2005**, *13* (3), 209–216. https://doi.org/10.1002/pip.626.

(5) Rau, U.; Jasenek, A.; Schock, H. W.; Engelhardt, F.; Meyer, T. Electronic Loss Mechanisms in Chalcopyrite Based Heterojunction Solar Cells. *Thin Solid Films* **2000**, *361–362*, 298–302. https://doi.org/10.1016/S0040-6090(99)00762-2.

(6) Gloeckler, M.; Sites, J. R. Efficiency Limitations for Wide-Band-Gap Chalcopyrite Solar Cells. *Thin Solid Films* **2005**, *480–481*, 241–245. https://doi.org/10.1016/j.tsf.2004.11.018.

(7) Chirilă, A.; Reinhard, P.; Pianezzi, F.; Bloesch, P.; Uhl, A. R.; Fella, C.; Kranz, L.; Keller, D.; Gretener, C.; Hagendorfer, H.; Jaeger, D.; Erni, R.; Nishiwaki, S.; Buecheler, S.; Tiwari, A. N. Potassium-Induced Surface Modification of Cu(In,Ga)Se_2 Thin Films for High-Efficiency Solar Cells. *Nature Materials* **2013**, *12* (12), 1107–1111. https://doi.org/10.1038/nmat3789.

(8) Jackson, P.; Hariskos, D.; Wuerz, R.; Kiowski, O.; Bauer, A.; Friedlmeier, T. M.; Powalla, M. Properties of Cu(In,Ga)Se $_2$ Solar Cells with New Record Efficiencies up to 21.7%: Properties of Cu(In,Ga)Se $_2$ Solar Cells with New Record Efficiencies up to 21.7%. *Phys. Status Solidi RRL* **2015**, *9* (1), 28–31. https://doi.org/10.1002/pssr.201409520.

(9) Jackson, P.; Hariskos, D.; Wuerz, R.; Wischmann, W.; Powalla, M. Compositional Investigation of Potassium Doped Cu(In,Ga)Se $_2$ Solar Cells with Efficiencies up to 20.8%: Compositional Investigation of Potassium Doped Cu(In,Ga)Se $_2$ Solar Cells with Efficiencies up to 20.8%. *Phys. Status Solidi RRL* **2014**, *8* (3), 219–222. https://doi.org/10.1002/pssr.201409040.

(10) Kamada, R.; Yagioka, T.; Adachi, S.; Handa, A.; Tai, K. F.; Kato, T.; Sugimoto, H. New World Record Cu(In, Ga)(Se, S)$_2$ Thin Film Solar Cell Efficiency beyond 22%. In *2016 IEEE 43rd Photovoltaic Specialists Conference (PVSC)*; 2016; pp 1287–1291. https://doi.org/10.1109/PVSC.2016.7749822.

(11) Jackson, P.; Wuerz, R.; Hariskos, D.; Lotter, E.; Witte, W.; Powalla, M. Effects of Heavy Alkali Elements in Cu(In,Ga)Se$_2$ Solar Cells with Efficiencies up to 22.6%. *physica status solidi (RRL) – Rapid Research Letters* **2016**, *10* (8), 583–586. https://doi.org/10.1002/pssr.201600199.

(12) Nakamura, M.; Yamaguchi, K.; Kimoto, Y.; Yasaki, Y.; Kato, T.; Sugimoto, H. Cd-Free Cu(In,Ga)(Se,S)$_2$ Thin-Film Solar Cell With Record Efficiency of 23.35%. *IEEE Journal of Photovoltaics* **2019**, *9* (6), 1863–1867. https://doi.org/10.1109/JPHOTOV.2019.2937218.

(13) Kato, T.; Wu, J.-L.; Hirai, Y.; Sugimoto, H.; Bermudez, V. Record Efficiency for Thin-Film Polycrystalline Solar Cells Up to 22.9% Achieved by Cs-Treated Cu(In,Ga)(Se,S)$_2$. *IEEE Journal of Photovoltaics* **2019**, *9* (1), 325–330. https://doi.org/10.1109/JPHOTOV.2018.2882206.

(14) Kanevce, A.; Paetel, S.; Hariskos, D.; Magorian Friedlmeier, T. Impact of RbF-PDT on Cu(In,Ga)Se $_2$ Solar Cells with CdS and Zn(O,S) Buffer Layers. *EPJ Photovolt.* **2020**, *11*, 8. https://doi.org/10.1051/epjpv/2020005.

(15) Siebentritt, S.; Avancini, E.; Bär, M.; Bombsch, J.; Bourgeois, E.; Buecheler, S.; Carron, R.; Castro, C.; Duguay, S.; Félix, R.; Handick, E.; Hariskos, D.; Havu, V.; Jackson, P.; Komsa, H.; Kunze, T.; Malitckaya, M.; Menozzi, R.; Nesladek, M.; Nicoara, N.; Puska, M.; Raghuwanshi, M.; Pareige, P.; Sadewasser, S.; Sozzi, G.; Tiwari, A. N.; Ueda, S.; Vilalta-Clemente, A.; Weiss, T. P.; Werner, F.; Wilks, R. G.; Witte, W.; Wolter, M. H. Heavy Alkali Treatment of Cu(In,Ga)Se $_2$ Solar Cells: Surface versus Bulk Effects. *Adv. Energy Mater.* **2020**, *10* (8), 1903752. https://doi.org/10.1002/aenm.201903752.

(16) Pianezzi, F.; Reinhard, P.; Chirilă, A.; Bissig, B.; Nishiwaki, S.; Buecheler, S.; Tiwari, A. N. Unveiling the Effects of Post-Deposition Treatment with Different Alkaline Elements on the Electronic Properties of CIGS Thin Film Solar Cells. *Phys. Chem. Chem. Phys.* **2014**, *16* (19), 8843. https://doi.org/10.1039/c4cp00614c.

(17) Aguiar, J. A.; Stokes, A.; Jiang, C.-S.; Aoki, T.; Kotula, P. G.; Patel, M. K.; Gorman, B.; Al-Jassim, M. Revealing Surface Modifications of Potassium-Fluoride-Treated Cu(In,Ga)Se_2: A Study of Material Structure, Chemistry, and Photovoltaic Performance. *Advanced Materials Interfaces* **2016**, *3* (17), 1600013. https://doi.org/10.1002/admi.201600013.

(18) Muzzillo, C. P.; Poplawsky, J. D.; Tong, H. M.; Guo, W.; Anderson, T. Revealing the Beneficial Role of K in Grain Interiors, Grain Boundaries, and at the Buffer Interface for Highly Efficient $CuInSe_2$ Solar Cells. *Progress in Photovoltaics: Research and Applications* **2018**, *26* (10), 825–834. https://doi.org/10.1002/pip.3022.

(19) Handick, E.; Reinhard, P.; Alsmeier, J.-H.; Köhler, L.; Pianezzi, F.; Krause, S.; Gorgoi, M.; Ikenaga, E.; Koch, N.; Wilks, R. G.; Buecheler, S.; Tiwari, A. N.; Bär, M. Potassium Postdeposition Treatment-Induced Band Gap Widening at Cu(In,Ga)Se_2 Surfaces – Reason for Performance Leap? *ACS Appl. Mater. Interfaces* **2015**, *7* (49), 27414–27420. https://doi.org/10.1021/acsami.5b09231.

(20) Schöppe, P.; Schönherr, S.; Jackson, P.; Wuerz, R.; Wisniewski, W.; Ritzer, M.; Zapf, M.; Johannes, A.; Schnohr, C. S.; Ronning, C. Overall Distribution of Rubidium in Highly Efficient Cu(In,Ga)Se_2 Solar Cells. *ACS Appl. Mater. Interfaces* **2018**, *10* (47), 40592–40598. https://doi.org/10.1021/acsami.8b16040.

(21) de Wild, J.; Buldu, D. G.; Schnabel, T.; Simor, M.; Kohl, T.; Birant, G.; Brammertz, G.; Meuris, M.; Poortmans, J.; Vermang, B. High Voc upon KF Post-Deposition Treatment for Ultrathin Single-Stage Coevaporated Cu(In, Ga)Se_2 Solar Cells. *ACS Appl. Energy Mater.* **2019**, *2* (8), 6102–6111. https://doi.org/10.1021/acsaem.9b01370.

(22) Jensen, S. A.; Glynn, S.; Kanevce, A.; Dippo, P.; Li, J. V.; Levi, D. H.; Kuciauskas, D. Beneficial Effect of Post-Deposition Treatment in High-Efficiency Cu(In,Ga)Se_2 Solar Cells through Reduced Potential Fluctuations. *J. Appl. Phys.* **2016**, *120* (6), 063106. https://doi.org/10.1063/1.4960344.

(23) Sun, Y.; Lin, S.; Li, W.; Cheng, S.; Zhang, Y.; Liu, Y.; Liu, W. Review on Alkali Element Doping in Cu(In,Ga)Se_2 Thin Films and Solar Cells. *Engineering* **2017**, *3* (4), 452–459. https://doi.org/10.1016/J.ENG.2017.04.020.

(24) Kiss, J.; Gruhn, T.; Roma, G.; Felser, C. Theoretical Study on the Structure and Energetics of Cd Insertion and Cu Depletion of $CuIn_5Se_8$. *J. Phys. Chem. C* **2013**, *117* (21), 10892–10900. https://doi.org/10.1021/jp312467f.

(25) Kohl, T.; Rivas, N. A.; de Wild, J.; Buldu, D. G.; Birant, G.; Brammertz, G.; Meuris, M.; Renner, F. U.; Poortmans, J.; Vermang, B. Inclusion of Water in Cu(In, Ga)Se_2 Absorber Material During Accelerated Lifetime Testing. *ACS Appl. Energy Mater.* **2020**, *3* (6), 5120–5125. https://doi.org/10.1021/acsaem.0c00610.

(26) Fthenakis, V. Sustainability of Photovoltaics: The Case for Thin-Film Solar Cells. *Renewable and Sustainable Energy Reviews* **2009**, *13* (9), 2746–2750.

(27) Gloeckler, M.; Sites, J. R. Potential of Submicrometer Thickness Cu(In,Ga)Se_2 Solar Cells. *Journal of Applied Physics* **2005**, *98* (10), 103703. https://doi.org/10.1063/1.2128054.

(28) Amin, N.; Chelvanathan, P.; Hossain, M. I.; Sopian, K. Numerical Modelling of Ultra Thin Cu(In,Ga)Se2 Solar Cells. *Energy Procedia* **2012**, *15*, 291–298. https://doi.org/10.1016/j.egypro.2012.02.034.

(29) Han, A.; Zhang, Y.; Song, W.; Li, B.; Liu, W.; Sun, Y. Structure, Morphology and Properties of Thinned Cu(In, Ga)Se_2 Films and Solar Cells. *Semicond. Sci. Technol.* **2012**, *27* (3), 035022. https://doi.org/10.1088/0268-1242/27/3/035022.

(30) Vermang, B.; Fjällström, V.; Pettersson, J.; Salomé, P.; Edoff, M. Development of Rear Surface Passivated Cu(In,Ga)Se_2 Thin Film Solar Cells with Nano-Sized Local Rear Point Contacts. *Solar Energy Materials and Solar Cells* **2013**, *117*, 505–511. https://doi.org/10.1016/j.solmat.2013.07.025.

(31) Kotipalli, R.; Delamare, R.; Poncelet, O.; Tang, X.; Francis, L. A.; Flandre, D. Passivation Effects of Atomic-Layer-Deposited Aluminum Oxide. *EPJ Photovolt.* **2013**, *4*, 45107. https://doi.org/10.1051/epjpv/2013023.

(32) Aberle, A. G.; Glunz, S.; Warta, W. Impact of Illumination Level and Oxide Parameters on Shockley–Read–Hall Recombination at the Si-SiO_2 Interface. *Journal of Applied Physics* **1992**, *71* (9), 4422–4431. https://doi.org/10.1063/1.350782.

(33) Dingemans, G.; Kessels, W. M. M. Status and Prospects of Al_2O_3 -Based Surface Passivation Schemes for Silicon Solar Cells. *Journal of Vacuum Science & Technology A: Vacuum, Surfaces, and Films* **2012**, *30* (4), 040802. https://doi.org/10.1116/1.4728205.

(34) Salomé, P. M. P.; Vermang, B.; Ribeiro-Andrade, R.; Teixeira, J. P.; Cunha, J. M. V.; Mendes, M. J.; Haque, S.; Borme, J.; Águas, H.; Fortunato, E.; Martins, R.; González, J. C.; Leitão, J. P.; Fernandes, P. A.; Edoff, M.; Sadewasser, S. Passivation of Interfaces in Thin Film Solar Cells: Understanding the Effects of a Nanostructured Rear Point Contact Layer. *Adv. Mater. Interfaces* **2018**, *5* (2), 1701101. https://doi.org/10.1002/admi.201701101.

(35) Vermang, B.; Watjen, J. T.; Frisk, C.; Fjallstrom, V.; Rostvall, F.; Edoff, M.; Salome, P.; Borme, J.; Nicoara, N.; Sadewasser, S. Introduction of Si PERC Rear Contacting Design to Boost Efficiency of Cu(In,Ga)Se $_2$ Solar Cells. *IEEE J. Photovoltaics* **2014**, *4* (6), 1644–1649. https://doi.org/10.1109/JPHOTOV.2014.2350696.

(36) Bose, S.; Cunha, J. M. V.; Borme, J.; Chen, W. C.; Nilsson, N. S.; Teixeira, J. P.; Gaspar, J.; Leitão, J. P.; Edoff, M.; Fernandes, P. A.; Salomé, P. M. P. A Morphological and Electronic Study of Ultrathin Rear Passivated Cu(In,Ga)Se_2 Solar Cells. *Thin Solid Films* **2019**, *671*, 77–84. https://doi.org/10.1016/j.tsf.2018.12.028.

(37) Cunha, J. M. V.; Fernandes, P. A.; Salome, P. M. P.; Lopes, T. S.; Bose, S.; Hultqvist, A.; Chen, W.-C.; Donzel-Gargand, O.; Ribeiro, R. M.; Oliveira, A. J. N.; Edoff, M. Decoupling of Optical and Electrical Properties of Rear Contact CIGS Solar Cells. *IEEE J. Photovoltaics* **2019**, *9* (6), 1857–1862. https://doi.org/10.1109/JPHOTOV.2019.2933357.

(38) Lopes, T. S.; Cunha, J. M. V.; Bose, S.; Barbosa, J. R. S.; Borme, J.; Donzel-Gargand, O.; Rocha, C.; Silva, R.; Hultqvist, A.; Chen, W.-C.; Silva, A. G.; Edoff, M.; Fernandes, P. A.; Salome, P. M. P. Rear Optical Reflection and Passivation Using a Nanopatterned Metal/Dielectric Structure in Thin-Film Solar Cells. *IEEE J. Photovoltaics* **2019**, *9* (5), 1421–1427. https://doi.org/10.1109/JPHOTOV.2019.2922323.

(39) Bose, S.; Cunha, J. M. V.; Suresh, S.; De Wild, J.; Lopes, T. S.; Barbosa, J. R. S.; Silva, R.; Borme, J.; Fernandes, P. A.; Vermang, B.; Salomé, P. M. P. Optical Lithography Patterning of SiO_2 Layers for Interface Passivation of Thin Film Solar Cells. *Sol. RRL* **2018**, *2* (12), 1800212. https://doi.org/10.1002/solr.201800212.

(40) Mollica, F.; Goffard, J.; Jubault, M.; Donsanti, F.; Collin, S.; Cattoni, A.; Lombez, L.; Naghavi, N. Comparative Study of Patterned TiO_2 and Al_2O_3 Layers as Passivated Back-Contact for Ultra-Thin Cu(In, Ga)Se_2 Solar Cells. In *2016 IEEE 43rd Photovoltaic Specialists Conference (PVSC)*; 2016; pp 2213–2217. https://doi.org/10.1109/PVSC.2016.7750028.

(41) Casper, P.; Hünig, R.; Gomard, G.; Kiowski, O.; Reitz, C.; Lemmer, U.; Powalla, M.; Hetterich, M. Optoelectrical Improvement of Ultra-Thin Cu(In,Ga)Se $_2$ Solar Cells through Microstructured MgF $_2$ and Al $_2$ O $_3$ Back Contact Passivation Layer. *Phys. Status Solidi RRL* **2016**, *10* (5), 376–380. https://doi.org/10.1002/pssr.201600018.

(42) de Wild, J.; Kohl, T.; Buldu, D. G.; Birant, G.; Parragh, D. M.; Brammertz, G.; Meuris, M.; Poortmans, J.; Vermang, B. KF Postdeposition Treatment in N_2 of Single-Stage Thin Cu(In,Ga)Se_2 Absorber Layers. *IEEE Journal of Photovoltaics* **2020**, *10* (1), 255–258. https://doi.org/10.1109/JPHOTOV.2019.2947758.

(43) Vermang, B.; Ren, Y.; Joel, J.; Frisk, C.; Donzel-Gargand, O.; Salomé, P.; Borme, J.; Sadewasser, S.; Platzer-Björkman, C.; Edoff, M. Rear Surface Optimization of CZTS Solar Cells by Use of a Passivation Layer with Nano-Sized Point Openings. In *2015 IEEE 42nd Photovoltaic Specialist Conference (PVSC)*; 2015; pp 1–3. https://doi.org/10.1109/PVSC.2015.7355624.

(44) Salomé, P.; Fjällström, V.; Hultqvist, A.; Edoff, M. Na Doping of CIGS Solar Cells Using Low Sodium-Doped Mo Layer. *IEEE Journal of Photovoltaics* **2013**, *3* (1), 509–513. https://doi.org/10.1109/JPHOTOV.2012.2226144.

(45) Salomé, P. M. P.; Hultqvist, A.; Fjällström, V.; Edoff, M.; Aitken, B. G.; Zhang, K.; Fuller, K.; Kosik Williams, C. Incorporation of Na in Cu(In,Ga)Se_2 Thin-Film Solar Cells: A Statistical Comparison Between Na From Soda-Lime Glass and From a Precursor Layer of NaF. *IEEE Journal of Photovoltaics* **2014**, *4* (6), 1659–1664. https://doi.org/10.1109/JPHOTOV.2014.2357261.

(46) de Wild, J.; Simor, M.; Buldu, D. G.; Kohl, T.; Brammertz, G.; Meuris, M.; Poortmans, J.; Vermang, B. Alkali treatment for single-stage co-evaporated thin $CuIn_{0.7}Ga_{0.3}Se_2$ solar cells. *Thin Solid Films* **2019**, *671*, 44–48. https://doi.org/10.1016/j.tsf.2018.12.022.

(47) Garud, S.; Gampa, N.; Allen, T. G.; Kotipalli, R.; Flandre, D.; Batuk, M.; Hadermann, J.; Meuris, M.; Poortmans, J.; Smets, A.; Vermang, B. Surface Passivation of CIGS Solar Cells

Using Gallium Oxide. *Phys. Status Solidi A* **2018**, *215* (7), 1700826. https://doi.org/10.1002/pssa.201700826.

(48) Burgelman, M.; Nollet, P.; Degrave, S. Modelling Polycrystalline Semiconductor Solar Cells. *Thin Solid Films* **2000**, *361–362*, 527–532. https://doi.org/10.1016/S0040-6090(99)00825-1.

(49) Friedlmeier, T. M.; Jackson, P.; Bauer, A.; Hariskos, D.; Kiowski, O.; Wuerz, R.; Powalla, M. Improved Photocurrent in Cu(In,Ga)Se $_2$ Solar Cells: From 20.8% to 21.7% Efficiency with CdS Buffer and 21.0% Cd-Free. *IEEE J. Photovoltaics* **2015**, *5* (5), 1487–1491. https://doi.org/10.1109/JPHOTOV.2015.2458039.

(50) Pettersson, J.; Platzer-Björkman, C.; Zimmermann, U.; Edoff, M. Baseline Model of Graded-Absorber Cu(In,Ga)Se_2 Solar Cells Applied to Cells with $Zn_{1-x}Mg_xO$ Buffer Layers. *Thin Solid Films* **2011**, *519* (21), 7476–7480. https://doi.org/10.1016/j.tsf.2010.12.141.

(51) Rincon, C.; Marquez, R. Defect Physics of the $CuInSe_2$ Chalcopyrite Semiconductor. *Journal of Physics and Chemistry of Solids* **1999**, 9.

(52) Carron, R.; Avancini, E.; Feurer, T.; Bissig, B.; Losio, P. A.; Figi, R.; Schreiner, C.; Bürki, M.; Bourgeois, E.; Remes, Z.; Nesladek, M.; Buecheler, S.; Tiwari, A. N. Refractive Indices of Layers and Optical Simulations of Cu(In,Ga)Se_2 Solar Cells. *Sci Technol Adv Mater* **2018**, *19* (1), 396–410. https://doi.org/10.1080/14686996.2018.1458579.

(53) Werner, W. S. M.; Glantschnig, K.; Ambrosch-Draxl, C. Optical Constants and Inelastic Electron-Scattering Data for 17 Elemental Metals. *Journal of Physical and Chemical Reference Data* **2009**, *38* (4), 1013–1092. https://doi.org/10.1063/1.3243762.

(54) Taretto, K.; Rau, U. Numerical Simulation of Carrier Collection and Recombination at Grain Boundaries in Cu(In,Ga)Se_2 Solar Cells. *Journal of Applied Physics* **2008**, *103* (9), 094523. https://doi.org/10.1063/1.2917293.

(55) Hegedus, S. S.; Shafarman, W. N. Thin-Film Solar Cells: Device Measurements and Analysis. *Progress in Photovoltaics: Research and Applications* **2004**, *12* (2–3), 155–176. https://doi.org/10.1002/pip.518.

(56) Photovoltaic Properties of Standard Devices. In *Chalcogenide Photovoltaics*; John Wiley & Sons, Ltd, 2011; pp 277–304. https://doi.org/10.1002/9783527633708.ch6.

(57) Salomé, P. M. P.; Fjallstrom, V.; Hultqvist, A.; Szaniawski, P.; Zimmermann, U.; Edoff, M. The Effect of Mo Back Contact Ageing on Cu(In,Ga)Se_2 Thin-Film Solar Cells. *Progress in Photovoltaics: Research and Applications* **2014**, *22* (1), 83–89. https://doi.org/10.1002/pip.2360.

(58) Umehara, T.; Nakada, K.; Yamada, A. Impact of Roll-over-Shaped Current–Voltage Characteristics and Device Properties of Ag(In,Ga)Se2 Solar Cells. *Jpn. J. Appl. Phys.* **2016**, *56* (1), 012302. https://doi.org/10.7567/JJAP.56.012302.

(59) Lundberg, O.; Bodegård, M.; Malmström, J.; Stolt, L. Influence of the Cu(In,Ga)Se_2 Thickness and Ga Grading on Solar Cell Performance. *Progress in Photovoltaics: Research and Applications* **2003**, *11* (2), 77–88. https://doi.org/10.1002/pip.462.

(60) Duchatelet, A.; Letty, E.; Jaime-Ferrer, S.; Grand, P.-P.; Mollica, F.; Naghavi, N. The Impact of Reducing the Thickness of Electrodeposited Stacked Cu/In/Ga Layers on the Performance of CIGS Solar Cells. *Solar Energy Materials and Solar Cells* **2017**, *162*, 114–119. https://doi.org/10.1016/j.solmat.2016.12.045.

(61) Sharaman, W. N.; Birkmire, R. W.; Marsillac, S.; Marudachalam, M.; Orbey, N.; Russell, T. W. F. Effect of Reduced Deposition Temperature, Time, and Thickness on Cu(InGa)Se_2 Films and Devices. In *Conference Record of the Twenty Sixth IEEE Photovoltaic Specialists Conference - 1997*; 1997; pp 331–334. https://doi.org/10.1109/PVSC.1997.654095.

(62) Shockley, W.; Read, W. T. Statistics of the Recombinations of Holes and Electrons. *Phys. Rev.* **1952**, *87* (5), 835–842. https://doi.org/10.1103/PhysRev.87.835.

(63) Hall, R. N. Electron-Hole Recombination in Germanium. *Phys. Rev.* **1952**, *87* (2), 387–387. https://doi.org/10.1103/PhysRev.87.387.

(64) Scheer, R. Towards an Electronic Model for $CuIn_{1-x}Ga_xSe_2$ Solar Cells. *Thin Solid Films* **2011**, *519* (21), 7472–7475. https://doi.org/10.1016/j.tsf.2011.01.092.

(65) Hilibrand, J.; Gold, R. Determination of the Impurity Distribution in Junction Diodes from Capacitance-Voltage Measurements. *RCA review* **1960**, *21* (2), 245–252.

(66) P-n Junctions. In *Physics of Semiconductor Devices*; John Wiley & Sons, Ltd, 2006; pp 77–133. https://doi.org/10.1002/9780470068328.ch2.

(67) Persson, C.; Zhao, Y.-J.; Lany, S.; Zunger, A. N -Type Doping of $CuInSe_2$ and $CuGaSe_2$. *Phys. Rev. B* **2005**, *72* (3), 035211. https://doi.org/10.1103/PhysRevB.72.035211.

(68) Kron, G.; Egerter, T.; Werner, J. H.; Rau, U. Electronic Transport in Dye-Sensitized Nanoporous TiO_2 Solar CellsComparison of Electrolyte and Solid-State Devices. *J. Phys. Chem. B* **2003**, *107* (15), 3556–3564. https://doi.org/10.1021/jp0222144.

(69) Yeum, B. Electrochemical Impedance Spectroscopy: Data Analysis Software, Ann Arbor, MI, USA, 2001.

(70) Cunha, J. M. V.; Rocha, C.; Vinhais, C.; Fernandes, P. A.; Salomé, P. M. P. Understanding the AC Equivalent Circuit Response of Ultrathin Cu(In,Ga)Se_2 Solar Cells. *IEEE Journal of Photovoltaics* **2019**, *9* (5), 1442–1448. https://doi.org/10.1109/JPHOTOV.2019.2927918.

(71) Proskuryakov, Y. Y.; Durose, K.; Taele, B. M.; Oelting, S. Impedance Spectroscopy of Unetched CdTe/CdS Solar Cells—Equivalent Circuit Analysis. *Journal of Applied Physics* **2007**, *102* (2), 024504. https://doi.org/10.1063/1.2757011.

(72) Fernandes, P. A.; Sartori, A. F.; Salomé, P. M. P.; Malaquias, J.; da Cunha, A. F.; Graça, M. P. F.; González, J. C. Admittance Spectroscopy of Cu_2ZnSnS_4 Based Thin Film Solar Cells. *Appl. Phys. Lett.* **2012**, *100* (23), 233504. https://doi.org/10.1063/1.4726042.

(73) Olayiwola, O. I.; Barendse, P. S. Dynamic Equivalent Circuit Modelling of Polycrystalline Silicon Photovoltaic Cells. In *2017 IEEE Energy Conversion Congress and Exposition (ECCE)*; 2017; pp 2310–2317. https://doi.org/10.1109/ECCE.2017.8096449.

(74) Yadav, P.; Pandey, K.; Tripathi, B.; Kumar, M. Investigation of Interface Limited Charge Extraction and Recombination in Polycrystalline Silicon Solar Cell: Using DC and AC Characterization Techniques. *Solar Energy* **2015**, *116*, 293–302. https://doi.org/10.1016/j.solener.2015.04.011.

(75) Tiwari, D.; Koehler, T.; Lin, X.; Sarua, A.; Harniman, R.; Wang, L.; Klenk, R.; Fermin, D. J. Single Molecular Precursor Solution for CuIn(S,Se) $_2$ Thin Films Photovoltaic Cells: Structure and Device Characteristics. *ACS Appl. Mater. Interfaces* **2017**, *9* (3), 2301–2308. https://doi.org/10.1021/acsami.6b12306.

(76) Roberts, G. I.; Crowell, C. R. Capacitance Energy Level Spectroscopy of Deep-Lying Semiconductor Impurities Using Schottky Barriers. *Journal of Applied Physics* **1970**, *41* (4), 1767–1776. https://doi.org/10.1063/1.1659102.

(77) P-n Junctions 222. In *Physics of Semiconductor Devices*; John Wiley & Sons, Ltd, 2006; pp 77–133. https://doi.org/10.1002/9780470068328.ch2.

(78) Mora-Seró, I.; Garcia-Belmonte, G.; Boix, P. P.; Vázquez, M. A.; Bisquert, J. Impedance Spectroscopy Characterisation of Highly Efficient Silicon Solar Cells under Different Light Illumination Intensities. *Energy Environ. Sci.* **2009**, *2* (6), 678–686. https://doi.org/10.1039/B812468J.

(79) Gupta, G. K.; Garg, A.; Dixit, A. Electrical and Impedance Spectroscopy Analysis of Sol-Gel Derived Spin Coated Cu_2ZnSnS_4 Solar Cell. *Journal of Applied Physics* **2018**, *123* (1), 013101. https://doi.org/10.1063/1.5002619.

(80) Schroder, K. Dieter. Semiconductor Material and Device Characterization, 3rd Edition | Wiley https://www.wiley.com/en-us/Semiconductor+Material+and+Device+Characterization%2C+3rd+Edition-p-9780471739067 (accessed Aug 27, 2020).

(81) Song, S. H.; Nagaich, K.; Aydil, E. S.; Feist, R.; Haley, R.; Campbell, S. A. Structure Optimization for a High Efficiency CIGS Solar Cell. In *2010 35th IEEE Photovoltaic Specialists Conference*; 2010; pp 002488–002492. https://doi.org/10.1109/PVSC.2010.5614724.

(82) Biercuk, M. J.; Monsma, D. J.; Marcus, C. M.; Becker, J. S.; Gordon, R. G. Low-Temperature Atomic-Layer-Deposition Lift-off Method for Microelectronic and Nanoelectronic Applications. *Appl. Phys. Lett.* **2003**, *83* (12), 2405–2407. https://doi.org/10.1063/1.1612904.

(83) Gokmen, T.; Gunawan, O.; Todorov, T. K.; Mitzi, D. B. Band Tailing and Efficiency Limitation in Kesterite Solar Cells. *Appl. Phys. Lett.* **2013**, *103* (10), 103506. https://doi.org/10.1063/1.4820250.

(84) Kuciauskas, D.; Li, J. V.; Contreras, M. A.; Pankow, J.; Dippo, P.; Young, M.; Mansfield, L. M.; Noufi, R.; Levi, D. Charge Carrier Dynamics and Recombination in Graded Band Gap $CuIn_{1-x}Ga_xSe_2$ Polycrystalline Thin-Film Photovoltaic Solar Cell Absorbers. *Journal of Applied Physics* **2013**, *114* (15), 154505. https://doi.org/10.1063/1.4825211.

(85) Kanevce, A.; Levi, D. H.; Kuciauskas, D. The Role of Drift, Diffusion, and Recombination in Time-Resolved Photoluminescence of CdTe Solar Cells Determined through Numerical Simulation. *Progress in Photovoltaics: Research and Applications* **2014**, *22* (11), 1138–1146. https://doi.org/10.1002/pip.2369.

(86) Oueslati, S.; Kauk-Kuusik, M.; Neubauer, C.; Mikli, V.; Meissner, D.; Brammertz, G.; Vermang, B.; Krustok, J.; Grossberg, M. Study of $(Ag_xCu_{1-x})2ZnSn(S,Se)_4$ Monograins Synthesized by Molten Salt Method for Solar Cell Applications. *Solar Energy* **2020**, *198*, 586–595. https://doi.org/10.1016/j.solener.2020.02.002.

(87) Gessert, T. A.; Dhere, R. G.; Duenow, J. N.; Kuciauskas, D.; Kanevce, A.; Bergeson, J. D. Comparison of Minority Carrier Lifetime Measurements in Superstrate and Substrate CdTe PV Devices. In *2011 37th IEEE Photovoltaic Specialists Conference*; 2011; pp 001271–001274. https://doi.org/10.1109/PVSC.2011.6186189.

(88) Hages, C. J.; Redinger, A.; Levcenko, S.; Hempel, H.; Koeper, M. J.; Agrawal, R.; Greiner, D.; Kaufmann, C. A.; Unold, T. Identifying the Real Minority Carrier Lifetime in Nonideal Semiconductors: A Case Study of Kesterite Materials. *Advanced Energy Materials* **2017**, *7* (18), 1700167. https://doi.org/10.1002/aenm.201700167.

(89) Teixeira, J. P.; Salomé, P. M. P.; Alves, B.; Edoff, M.; Leitão, J. P. Evidence of Limiting Effects of Fluctuating Potentials on Cu,In,Ga,Se_2 Thin-Film Solar Cells. *Phys. Rev. Applied* **2019**, *11* (5), 054013. https://doi.org/10.1103/PhysRevApplied.11.054013.

(90) Nikolaeva, A.; Krause, M.; Schäfer, N.; Witte, W.; Hariskos, D.; Kodalle, T.; Kaufmann, C. A.; Barreau, N.; Abou-Ras, D. Electrostatic Potential Fluctuations and Light-Soaking Effects in Cu(In,Ga)Se_2 Solar Cells. *Progress in Photovoltaics: Research and Applications* **2020**, *n/a* (n/a). https://doi.org/10.1002/pip.3299.

(91) Ghorbani, E.; Kiss, J.; Mirhosseini, H.; Roma, G.; Schmidt, M.; Windeln, J.; Kühne, T. D.; Felser, C. Hybrid-Functional Calculations on the Incorporation of Na and K Impurities into the $CuInSe_2$ and $CuIn_5Se_8$ Solar-Cell Materials. *J. Phys. Chem. C* **2015**, *119* (45), 25197–25203. https://doi.org/10.1021/acs.jpcc.5b07639.

(92) Lontchi, J.; Zhukova, M.; Kovacic, M.; Krc, J.; Chen, W.-C.; Edoff, M.; Bose, S.; Salomé, P. M. P.; Goffard, J.; Cattoni, A.; Gouillart, L.; Collin, S.; Gusak, V.; Flandre, D. Optimization of Back Contact Grid Size in Al $_2$O $_3$-Rear-Passivated Ultrathin CIGS PV Cells by 2-D Simulations. *IEEE Journal of Photovoltaics* **2020**, *10* (6), 1908–1917. https://doi.org/10.1109/JPHOTOV.2020.3012631.

(93) Reinhard, P.; Bissig, B.; Pianezzi, F.; Avancini, E.; Hagendorfer, H.; Keller, D.; Fuchs, P.; Döbeli, M.; Vigo, C.; Crivelli, P.; Nishiwaki, S.; Buecheler, S.; Tiwari, A. N. Features of KF

and NaF Postdeposition Treatments of Cu(In,Ga)Se $_2$ Absorbers for High Efficiency Thin Film Solar Cells. *Chem. Mater.* **2015**, *27* (16), 5755–5764. https://doi.org/10.1021/acs.chemmater.5b02335.

(94) Handick, E.; Reinhard, P.; Wilks, R. G.; Pianezzi, F.; Kunze, T.; Kreikemeyer-Lorenzo, D.; Weinhardt, L.; Blum, M.; Yang, W.; Gorgoi, M.; Ikenaga, E.; Gerlach, D.; Ueda, S.; Yamashita, Y.; Chikyow, T.; Heske, C.; Buecheler, S.; Tiwari, A. N.; Bär, M. Formation of a K-In-Se Surface Species by NaF/KF Postdeposition Treatment of Cu(In,Ga)Se_2 Thin-Film Solar Cell Absorbers. *ACS applied materials & interfaces* **2017**, *9* (4), 3581–3589. https://doi.org/10.1021/acsami.6b11892.

(95) Yang, P.; Wilks, R. G.; Yang, W.; Bär, M. Interface Formation between CdS and Alkali Postdeposition-Treated Cu(In,Ga)Se $_2$ Thin-Film Solar Cell Absorbers—Key To Understanding the Efficiency Gain. *ACS Appl. Mater. Interfaces* **2020**, *12* (5), 6688–6698. https://doi.org/10.1021/acsami.9b20327.

(96) Weiss, T. P.; Nishiwaki, S.; Bissig, B.; Carron, R.; Avancini, E.; Löckinger, J.; Buecheler, S.; Tiwari, A. N. Injection Current Barrier Formation for RbF Postdeposition-Treated Cu(In,Ga)Se_2-Based Solar Cells. *Advanced Materials Interfaces* **2018**, *5* (4), 1701007. https://doi.org/10.1002/admi.201701007.

(97) Curado, M. A.; Teixeira, J. P.; Monteiro, M.; Ribeiro, E. F. M.; Vilão, R. C.; Alberto, H. V.; Cunha, J. M. V.; Lopes, T. S.; Oliveira, K.; Donzel-Gargand, O.; Hultqvist, A.; Calderon, S.; Barreiros, M. A.; Chiappim, W.; Leitão, J. P.; Silva, A. G.; Prokscha, T.; Vinhais, C.; Fernandes, P. A.; Salomé, P. M. P. Front Passivation of Cu(In,Ga)Se_2 Solar Cells Using Al_2O_3: Culprits and

Benefits. *Applied Materials Today* **2020**, *21*, 100867. https://doi.org/10.1016/j.apmt.2020.100867.

(98) Han, J.; Liao, C.; Cha, L.; Jiang, T.; Xie, H.; Zhao, K.; Besland, M.-P. TEM and XPS Studies on CdS/CIGS Interfaces. *Journal of Physics and Chemistry of Solids* **2014**, *75* (12), 1279–1283. https://doi.org/10.1016/j.jpcs.2014.06.002.

(99) Salome, P. M. P.; Ribeiro-Andrade, R.; Teixeira, J. P.; Keller, J.; Torndahl, T.; Nicoara, N.; Edoff, M.; Gonzalez, J. C.; Leitao, J. P.; Sadewasser, S. Cd and Cu Interdiffusion in Cu(In, Ga)Se $_2$ /CdS Hetero-Interfaces. *IEEE J. Photovoltaics* **2017**, *7* (3), 858–863. https://doi.org/10.1109/JPHOTOV.2017.2666550.

(100) Abou-Ras, D.; Kostorz, G.; Romeo, A.; Rudmann, D.; Tiwari, A. N. Structural and Chemical Investigations of CBD- and PVD-CdS Buffer Layers and Interfaces in Cu(In,Ga)Se_2-Based Thin Film Solar Cells. *Thin Solid Films* **2005**, *480–481*, 118–123. https://doi.org/10.1016/j.tsf.2004.11.033.

(101) Muzzillo, C. P. Review of Grain Interior, Grain Boundary, and Interface Effects of K in CIGS Solar Cells: Mechanisms for Performance Enhancement. *Solar Energy Materials and Solar Cells* **2017**, *172*, 18–24. https://doi.org/10.1016/j.solmat.2017.07.006.

(102) Gunning, H. E.; Gordon, A. R. The Conductance and Ionic Mobilities for Aqueous Solutions of Potassium and Sodium Chloride at Temperatures from 15° to 45°C. *J. Chem. Phys.* **1942**, *10* (2), 126–131. https://doi.org/10.1063/1.1723667.

(103) Yamamoto, Y.; Yamamoto, K. Precise XPS Depth Profile of Soda-Lime-Silica Glass Using C_{60} Ion Beam. *Journal of Non-Crystalline Solids* **2010**, *356* (1), 14–18. https://doi.org/10.1016/j.jnoncrysol.2009.09.027.

(104) Shin, D.; Kim, J.; Gershon, T.; Mankad, R.; Hopstaken, M.; Guha, S.; Ahn, B. T.; Shin, B. Effects of the Incorporation of Alkali Elements on Cu(In,Ga)Se2 Thin Film Solar Cells. *Solar Energy Materials and Solar Cells* **2016**, *157*, 695–702. https://doi.org/10.1016/j.solmat.2016.07.015.

(105) Salomé, P. M. P.; Rodriguez-Alvarez, H.; Sadewasser, S. Incorporation of Alkali Metals in Chalcogenide Solar Cells. *Solar Energy Materials and Solar Cells* **2015**, *143*, 9–20. https://doi.org/10.1016/j.solmat.2015.06.011.

(106) Kirchartz, T.; Ding, K.; Rau, U. Fundamental Electrical Characterization of Thin-Film Solar Cells. In *Advanced Characterization Techniques for Thin Film Solar Cells*; John Wiley & Sons, Ltd, 2011; pp 33–60. https://doi.org/10.1002/9783527636280.ch2.

(107) Rau, U. Tunneling-Enhanced Recombination in Cu(In, Ga)Se_2 Heterojunction Solar Cells. *Appl. Phys. Lett.* **1999**, *74* (1), 111–113. https://doi.org/10.1063/1.122967.